Progress In Electromagnetics Research M, Vol. 53, 77–87, 2017

Enhanced Three-Dimensional Imaging for Multi-Circular Synthetic Aperture Radar

Lingjuan Yu[1, 2, *], Yun Lin[1], Qian Bao[1], Wenjie Shen[1], Yue Zhao[1], and Wen Hong[1]

Abstract—In multi-circular synthetic aperture radar (MCSAR) mode, resolution and sidelobes are two important parameters to consider when representing imaging quality, as in other SAR imaging modes. In this paper, three-dimensional (3-D) resolution and cone-shaped sidelobes of MCSAR are analyzed for a point target in the scene center under the Nyquist sampling criterion. The results of the analysis show that resolution can be improved, and cone-shaped sidelobes can be suppressed by increasing the system bandwidth and the length of synthetic aperture in the elevation direction. But this will make the system of acquiring data more difficult. It turns out that some digital signal processing techniques can enhance 3-D imaging quality of MCSAR. In this paper, a simple method based on spectrum extrapolation and interferometric phase masking is proposed to improve 3-D resolution and suppress cone-shaped sidelobes of MCSAR. Experimental results regarding a tank model in a microwave anechoic chamber demonstrate that this method is effective.

1. INTRODUCTION

Multi-circular synthetic aperture radar (MCSAR) is an extension of circular synthetic aperture radar (CSAR) [1–3]. MCSAR is an imaging mode where radar illuminates the target over multi-circular tracks [4–6]. It has the potential to produce high quality three-dimensional (3-D) images. As in other SAR imaging modes, resolution and sidelobes are two important parameters for representing imaging quality. In MCSAR mode, 3-D resolution and cone-shaped sidelobes are considered. The 3-D resolution can be analyzed from point spread function (PSF) and spectrum [7]. The cone-shaped sidelobes are always considered due to non-uniform sampling and undersampling in the elevation direction [7, 8]. In fact, even though the elevation acquisition strictly satisfies the Nyquist sampling criterion, cone-shaped sidelobes still exist. In this paper, we analyze resolution and cone-shaped sidelobes from the 3-D spectrum under the Nyquist sampling criterion. The results of the analysis on 3-D resolution and cone-shaped sidelobes of MCSAR show that resolution can be improved and cone-shaped sidelobes can be suppressed by increasing the system bandwidth and the length of synthetic aperture in the elevation direction. But this will make the system of acquiring data more difficult.

However, some digital signal processing techniques can be used to improve 3-D resolution and suppress cone-shaped sidelobes of MCSAR. Compressive sensing (CS) is a good way to reconstruct 3-D targets [9, 10]. It not only has the ability of super-resolution imaging, but also can suppress cone-shaped sidelobes by choosing strong scatterers of targets. The disadvantages of this method are that it is time-consuming and memory-consuming. CS used in the height reconstruction is also considered [7, 8], but it is still time-consuming. Besides, the whole aperture is divided into several sub-apertures, and the approximation is required in each sub-aperture reconstruction. In order to obtain 3-D reconstruction effectively, some classic processing techniques can be considered. As we

Received 3 November 2016, Accepted 30 December 2016, Scheduled 14 January 2017

* Corresponding author: Lingjuan Yu (yljsmile@163.com).

[1] National Key Laboratory of Science and Technology on Microwave Imaging, Institute of Electronics, Chinese Academy of Science, Beijing, China. [2] School of Information Engineering, Jiangxi University of Science and Technology, Ganzhou, China.

know, the spectrum extrapolation is a simple and effective method to increase the system bandwidth in CSAR mode [11]; the interferometric phase masking method in all-aperture is introduced to obtain the height of the target by suppressing cone-shaped sidelobes in two-pass CSAR mode [12]. Both of these methods can be extended to MCSAR mode. In this paper, we combine the spectrum extrapolation with the interferometric phase masking method to obtain high quality 3-D images. Experimental results regarding a tank model in a microwave anechoic chamber demonstrate that this method is effective.

The rest of the paper is organized as follows. In Section 2, the 3-D resolution analytical expressions are given, and the characteristics of cone-shaped sidelobes are analyzed. In Section 3, an enhanced imaging method based on spectrum extrapolation and interferometric phase masking is proposed. Experimental results are shown in Section 4. Finally, Section 5 concludes the paper.

2. THREE-DIMENSIONAL RESOLUTION AND CONE-SHAPED SIDELOBES OF MCSAR

The MCSAR imaging geometry is shown in Fig. 1. Radar illuminates the target area over multi-circular tracks. The distance between radar and the center of the target area is always a constant R_c. Assume that there are M tracks, the depression angle is θ and the depression angle sample spacing is $\Delta\theta$. Then the slant depression angle of the i-th track can be expressed as $\theta_i = \theta_1 + (i-1)\Delta\theta$, for $i = 1, 2, \ldots, M$. Furthermore, denote the azimuthal angle of radar as ϕ. Then the 3-D coordinates of the radar are $(x, y, z) = (R_c \cos\theta \cos\phi, R_c \cos\theta \sin\phi, R_c \sin\theta)$.

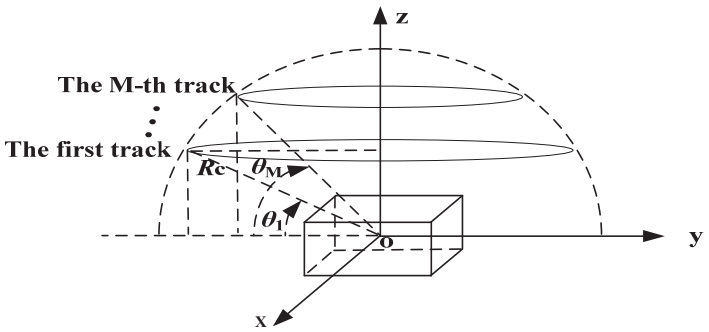

Figure 1. The MCSAR imaging geometry.

Suppose that there are N targets, the n-th target is located at (x_n, y_n, z_n), and its ideal reflectivity is σ_n. The echoed signals received by radar from these targets can be written as

$$s(k, \phi, \theta) = \sum_n \sigma_n \exp\left\{-j2k\sqrt{(x_n - x)^2 + (y_n - y)^2 + (z_n - z)^2}\right\} \tag{1}$$

where $k = 2\pi/\lambda$ and λ is the wavelength of transmitted signals.

2.1. Three-dimensional Resolution of MCSAR

From Eq. (1), the phase of the echoed signal about the n-th target is

$$phase_n = -2k\sqrt{(x_n - x)^2 + (y_n - y)^2 + (z_n - z)^2} \tag{2}$$

The spatial frequency in the k_x, k_y, k_z directions of the n-th target can be respectively derived as the derivative of the phase with respect to x, y, z [2],

$$\begin{cases} k_x = \dfrac{\partial(phase_n)}{\partial x} = 2k\dfrac{(x_n - R_c\cos\theta\cos\phi)}{R_n} \\ k_y = \dfrac{\partial(phase_n)}{\partial y} = 2k\dfrac{(y_n - R_c\cos\theta\sin\phi)}{R_n} \\ k_z = \dfrac{\partial(phase_n)}{\partial z} = 2k\dfrac{(z_n - R_c\sin\theta)}{R_n} \end{cases} \tag{3}$$

where $R_n = \sqrt{(x_n - R_c\cos\theta\cos\phi)^2 + (y_n - R_c\cos\theta\sin\phi)^2 + (z_n - R_c\sin\theta)^2}$.

We consider the spatial spectrum of the point target located at the origin ($x_n = y_n = z_n = 0$). Suppose that there are spatial spectrum overlaps in the k_z direction between two adjacent tracks. This means $2k_{\min}\sin\theta_{i+1} < 2k_{\max}\sin\theta_i$ ($k_{\min} = \min\{k\}$, $k_{\max} = \max\{k\}$ and $i = 1, 2, \ldots, M-1$). The 3-D spatial spectrum is shown in Fig. 2(a). The different colors in this figure represent the spatial spectrum of different tracks. The projection of the 3-D spatial spectrum onto k_xk_y plane is shown in Fig. 2(b). The projection of the 3-D spatial spectrum onto the k_xk_z plane is shown in Fig. 2(c).

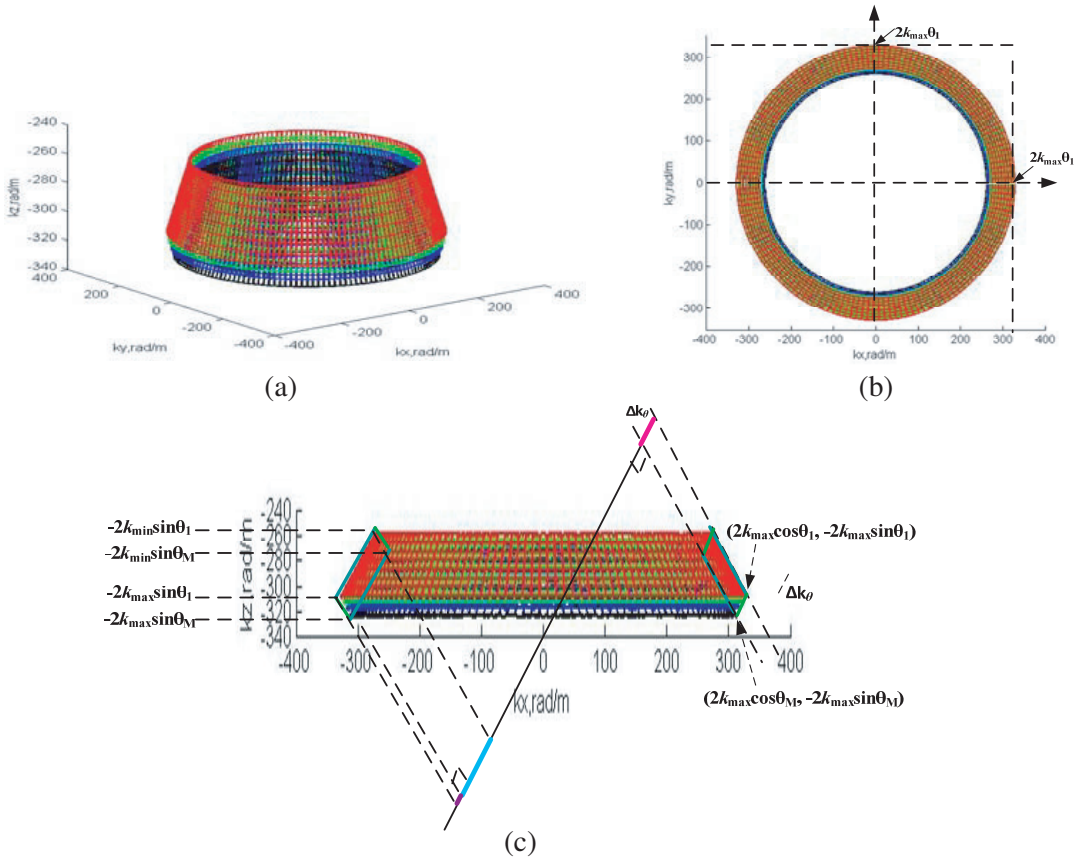

Figure 2. (a) 3-D spatial spectrum. (b) The projection of the 3-D spatial spectrum onto k_xk_y plane. (c) The projection of the 3-D spatial spectrum onto k_xk_z plane and onto the line with slope $\cot\theta_{av}$.

In Fig. 2, it is easy to obtain the width of the spatial spectrum in k_x, k_y, k_z directions. Thus analytical expressions of resolution in the x, y, z directions can be written as

$$\begin{cases} \Delta x = \Delta y \approx \dfrac{\pi}{2k_{\max}\cos\theta_1} \\ \Delta z \approx \dfrac{\pi}{k_{\max}\sin\theta_M - k_{\min}\sin\theta_1} \end{cases} \tag{4}$$

From Eq. (4), the resolution in the z direction can be improved by increasing the system bandwidth BW (where $BW = k_{\max} - k_{\min}$). The resolution in the x, y directions can also be improved slightly. In [4], the increased system bandwidth is also helpful to reduce the peak sidelobe ratio (PSLR) in the x, y directions.

2.2. Cone-shaped Sidelobes

With the 3-D spatial spectrum shown in Fig. 2(a), the PSF can be obtained by its inverse Fourier transform, which is shown in Fig. 3(a). The xz profile ($y = 0$) of the PSF is shown in Fig. 3(b). When

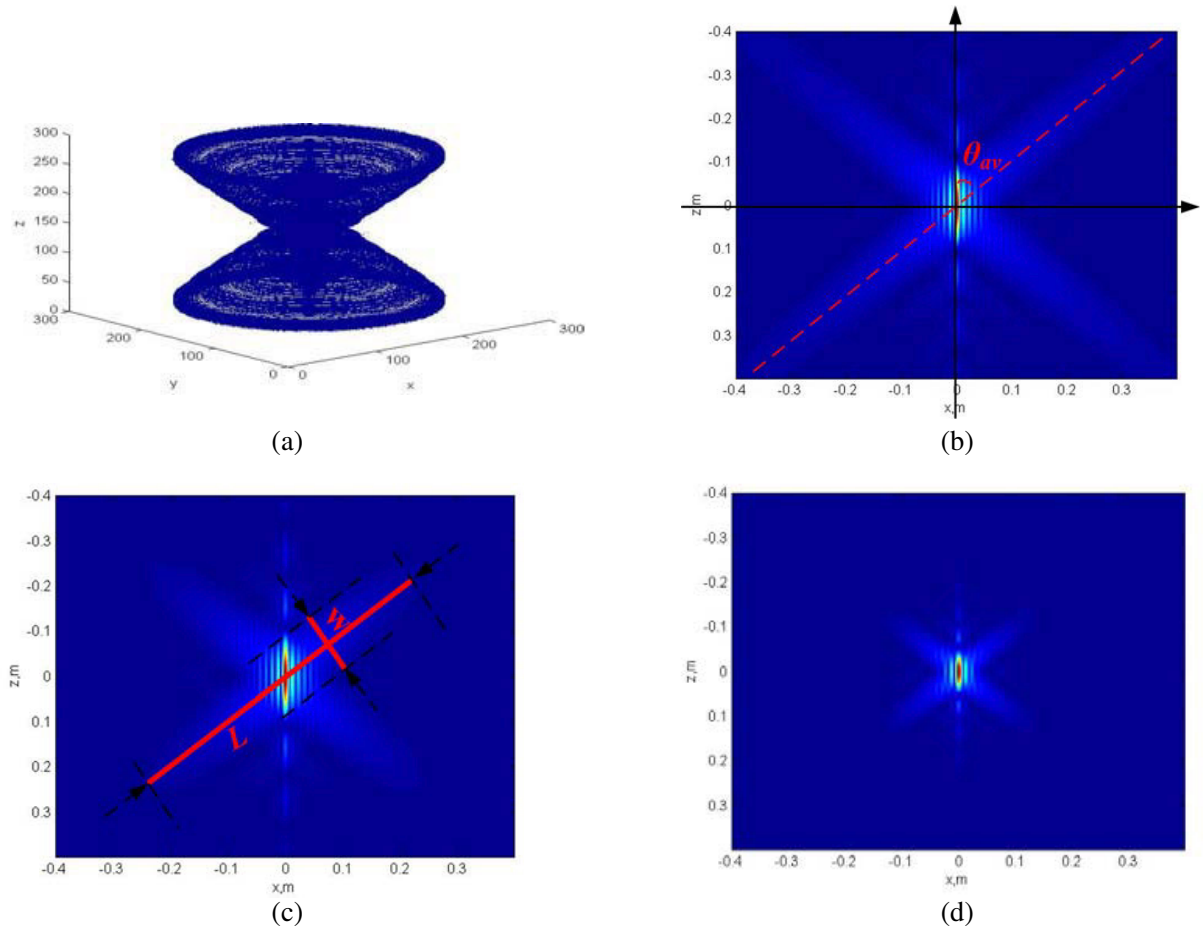

Figure 3. (a) 3-D PSF (the number of tracks is M, and the system bandwidth is BW). (b) The xz profile ($y = 0$) (the number of tracks is M, and the system bandwidth is BW). (c) The xz profile ($y = 0$) (the number of tracks is $2M$, and the system bandwidth is BW). (d) The xz profile ($y = 0$) (the number of tracks is $4M$, and the system bandwidth is $2BW$).

the number of tracks is increased to $2M$, and the system bandwidth is still BW, the xz profile ($y = 0$) is shown in Fig. 3(c). When the number of tracks is increased to $4M$, and the system bandwidth is increased to $2BW$, the xz profile ($y = 0$) is shown in Fig. 3(d). In all these figures, the cone-shaped sidelobes can be seen as the defocused imaging results of the point target located at the origin.

In Fig. 3(c), two solid lines in red are drawn along cone-shaped sidelobes. The slope of one line with length L is about $\cot\theta_{av}$ ($\theta_{av} \approx (\theta_1 + \theta_M)/2$) and the slope of the other line with length W is about $-\tan\theta_{av}$. The lengths L and W are defined as the length and the width of cone-shaped sidelobes respectively.

From Figs. 3(b)–(d), it is obvious that the length of the cone-shaped sidelobes is shorter when the number of tracks is bigger, and the width of the cone-shaped sidelobes is narrower when the system bandwidth is wider. These characteristics of cone-shaped sidelobes can be explained by considering the perspective of the spatial spectrum.

In order to illustrate the characteristic of the length of cone-shaped sidelobes, the 3-D spatial spectrum is projected onto the line with slope $\cot\theta_{av}$ which is on the $k_x k_z$ plane ($k_y = 0$). This is shown in Fig. 2(c). In this figure, the slope of the baselines ($\phi = 0°$) is also approximately equal to

$$\frac{-2k_{\max}\sin\theta_1 + 2k_{\max}\sin\theta_M}{2k_{\max}\cos\theta_1 - 2k_{\max}\cos\theta_M} \approx \cot\theta_{av} \tag{5}$$

Therefore, the width of the projected spectrum in pink is approximately equal to the spectrum

width Δk_θ in the direction of the baselines and it can be computed as

$$\begin{aligned}\Delta k_\theta &\approx \sqrt{(2k_{\max}\cos\theta_1 - 2k_{\max}\cos\theta_M)^2 + (2k_{\max}\sin\theta_1 - 2k_{\max}\sin\theta_M)^2} \\ &\approx 2k_{\max}\sin\left(\frac{M-1}{2}\Delta\theta\right)\end{aligned} \tag{6}$$

In addition, the width of the projected spectrum in purple is so narrow that it can be ignored and the width of the projected spectrum in green is approximately equal to the system bandwidth. On the other hand, the amplitudes of the projected spectrum in pink and in green decrease linearly, while the amplitude of the projected spectrum in black in the middle part is a constant.

As a result, the spectrum amplitudes on the line with slope $\cot\theta_{av}$ can be shown in Fig. 4. On the left side of Fig. 4, it is approximately trapezoidal shaped. On the right side of Fig. 4, the trapezoidal-shaped spectrum can be seen as the convolution of two rectangular-shaped spectra. According to the property of Fourier transform, the total spatial response of cone-shaped sidelobes in the direction of the line with slope $\cot\theta_{av}$ can be seen to be the product of two sinc function responses.

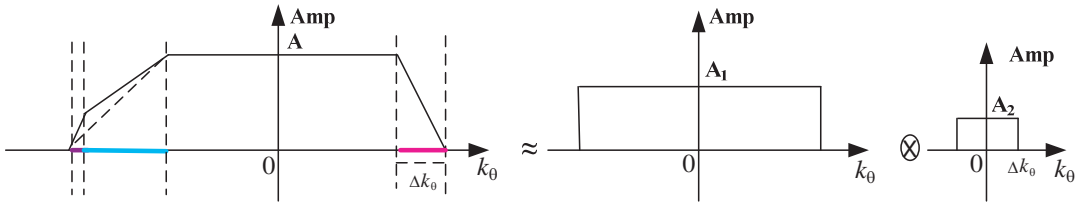

Figure 4. Spectrum amplitude on the line with the slope of $\cot\theta_{av}$ and its decomposition.

Because the spectrum width in the direction of the baselines is generally narrower than the system bandwidth, the sinc function corresponding to the rectangular-shaped spectrum with narrow width Δk_θ determines the amplitude of the total response. Thus the length of the cone-shaped sidelobes can be approximately defined as

$$L \approx \frac{2\pi}{\Delta k_\theta} \approx \frac{\pi}{k_{\max}\sin\left(\frac{M-1}{2}\Delta\theta\right)} \tag{7}$$

From Eq. (7), the length of cone-shaped sidelobes can be reduced by increasing the number of circular tracks under the Nyquist sampling criterion.

Similarly, when the 3-D spatial spectrum is projected onto the line with slope $-\tan\theta_{av}$ which is on the k_xk_z plane ($k_y = 0$), the width of the cone-shaped sidelobes can be approximately defined as

$$W \approx \frac{2\pi}{BW} = \frac{2\pi}{k_{\max} - k_{\min}} \tag{8}$$

From Eq. (8), the width of cone-shaped sidelobes can be reduced by increasing the system bandwidth BW.

The above method can also be used when analyzing the length of sidelobes in the x, y, z directions. This results in reducing the length of sidelobes in these directions by increasing the number of circular tracks. As expected, the length of sidelobes in z direction is changing, which is obvious from Figs. 3(b)–(d).

Under the Nyquist sampling criterion, increasing the number of circular tracks is the same as increasing the length of synthetic aperture in the elevation direction. Although the cone-shaped sidelobes can be suppressed by increasing the system bandwidth and the length of synthetic aperture in the elevation direction, it will make acquiring data more difficult.

3. ENHANCED 3-D IMAGING BASED ON SPECTRUM EXTRAPOLATION AND INTERFEROMETRIC PHASE MASKING

In this section, an enhanced 3-D imaging method based on spectrum extrapolation and interferometric phase masking is proposed to improve 3-D imaging quality.

3.1. The Principle of Spectrum Extrapolation

The spectrum extrapolation based on an autoregressive (AR) model is considered here. An AR model can make use of the correlation of the observed spectrum data. It is useful in super-resolution imaging of targets which are made up of strong scatterers.

Let $\{x(n),\, n = 1, 2, \ldots, N\}$ be the one-dimensional spectrum data. The forward prediction of $x(n)$ based on the p-th order AR model can be defined by [13, 14]

$$\hat{x}_f^p(n) = -\sum_{i=1}^{p} a_i x(n-i) \tag{9}$$

and the backward prediction of $x(n)$ can be defined by

$$\hat{x}_b^p(n-p) = -\sum_{i=1}^{p} a_i^* x(n-p+i) \tag{10}$$

where a_i denotes the i-th coefficient in the model, and $n = p+1, p+2, \ldots, N$.

Then the forward and backward prediction error can be expressed as

$$\begin{cases} e_f^p(n) = x(n) - \hat{x}_f^p(n) \\ e_b^p(n) = x(n-p) - \hat{x}_b^p(n-p) \end{cases} \tag{11}$$

By the minimization of forward and backward prediction error, that is $\{\min \sum_{n=p+1}^{N} (|e_f^p(n)|^2 + |e_b^p(n)|^2)/2\}$, the coefficients a_i can be obtained. With these coefficients, the width of the spectrum can be increased through Eqs. (9) and (10). The process of spectrum extrapolation is shown in Fig. 5.

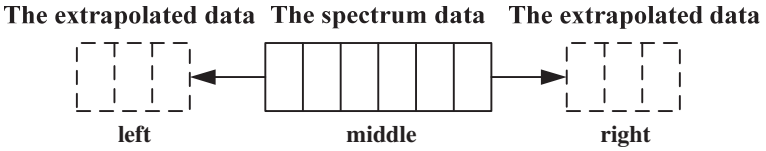

Figure 5. The process of spectrum extrapolation.

3.2. The Principle of Interferometric Phase Masking

The height reconstruction by interferometric phase masking is deduced in [12]. In this section, we simplify the derivation process. The imaging geometry of two adjacent circular tracks is shown in Fig. 6. Suppose that a point target is located at $(x_n,\, y_n,\, z_n)$, the azimuthal angle of radar is ϕ_1 the first depression angle is θ_1 and the second one is θ_2. Then the difference between two depression angles is $\Delta\theta$ $(\Delta\theta = \theta_2 - \theta_1)$.

We consider the two-dimensional (2-D) imaging at the same imaging plane for echoed signals from two adjacent tracks. Choose z_{plan} to be the height of imaging plane. When radar is in the first track, the 2-D imaging result on the plane of height z_{plan} is denoted by s_1 and the imaging positions of the point target can be obtained by

$$\begin{cases} x_{n1} \approx x_n + (z_n - z_{plan}) \tan\theta_1 \cos\phi_1 \\ y_{n1} \approx y_n + (z_n - z_{plan}) \tan\theta_1 \sin\phi_1 \end{cases} \tag{12}$$

When radar is in the second track, the 2-D imaging result on the plane of height z_{plan} is denoted by s_2 and the imaging positions of the point target can be obtained by

$$\begin{cases} x_{n2} \approx x_n + (z_n - z_{plan}) \tan\theta_2 \cos\phi_1 \\ y_{n2} \approx y_n + (z_n - z_{plan}) \tan\theta_2 \sin\phi_1 \end{cases} \tag{13}$$

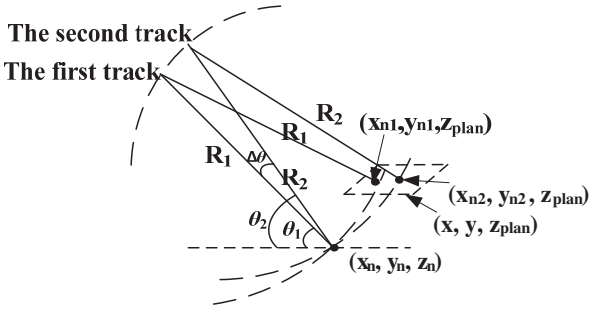

Figure 6. The imaging geometry of two adjacent circular tracks.

Both $(x_{n1},\ y_{n1})$ and $(x_{n2},\ y_{n2})$ fall in the same pixel unit $(x,\ y)$ to ensure that s_1 and s_2 are coherent. So the phase difference between s_1 and s_2 in the pixel unit $(x,\ y)$ is

$$\begin{aligned}\Delta\phi &\approx -\frac{4\pi}{\lambda}\sqrt{(x_{n1}-x_{n2})^2+(y_{n1}-y_{n2})^2}\cos\theta_{av} \\ &= -\frac{4\pi}{\lambda}(z_n-z_{plan})(\tan\theta_2-\tan\theta_1)\cos\theta_{av} \approx -\frac{4\pi\Delta\theta}{\lambda\cos\theta_{av}}(z_n-z_{plan})\end{aligned} \tag{14}$$

where $\theta_{av}\approx(\theta_1+\theta_2)/2$.

From Eq. (14), when the height of imaging plane z_{plan} is equal to the real height z_n, the phase difference is approximately equal to zero. Otherwise, it is not equal to zero. Therefore, the focused 2-D image can be achieved by discarding the pixel units where the phase difference is not approximately equal to zero. The processing is as follows.

At first, the phase difference can be obtained by

$$\Delta\phi = angle(s_1\ \cdot\ conj(s_2)) \tag{15}$$

where $angle(\bullet)$ represents the interferometric phase between s_1 and s_2.

Then the mask using interferometric phase can be designed as

$$mask=\begin{cases}1, & \Delta\phi\approx 0\\ 0, & otherwise\end{cases} \tag{16}$$

Finally, if s_1 or s_2 is multiplied by the mask, then a new image is obtained, where targets are focused because they are with the real height.

For two coherent 3-D images, take them as multi-slice 2-D images in the height direction, and do the interferometric phase masking at the same slice. Form a 3-D mask by determining whether interferometric phase is approximately zero at each slice. Then multiply one of the two images by the mask to obtain a focused 3-D image. In MCSAR mode, this method is very helpful to suppress cone-shaped sidelobes which are defocused imaging results of targets.

3.3. An Enhanced 3-D Imaging Method Based on Spectrum Extrapolation and Interferometric Phase Masking

Combining the spectrum extrapolation with interferometric phase masking, an enhanced imaging method is proposed to improve 3-D resolution and suppress cone-shaped sidelobes. The detailed steps of the method are as follows.

(1) Implement pulse compression, spectrum extrapolation based on an AR model and 3-D imaging using a back projection (BP) algorithm, for echoed signals received from each circular track. Denote the 3-D image of the i-th track as $S_i\,(i=1,2,\ldots,M)$.

(2) Calculate the interferometric phase $\Delta\phi_j\,(j=1,2,\ldots,M-1)$ for two 3-D images S_j and S_{j+1} by $\Delta\phi_j = angle(S_j\ \cdot\ conj(S_{j+1}))$. If $\Delta\phi_j$ is equal to zero, then $mask_j$ is equal to 1, otherwise, $mask_j$ is equal to 0. Multiply the first 3-D image S_j by the $mask_j$ to obtain a new focused 3-D image S_{j_new}, and the calculation expression is $S_{j\_new}=S_j\cdot mask_j$.

(3) Coherently add all the new focused 3-D images $S_{j\_new}\,(j = 1, 2, \ldots, M-1)$ to achieve the final MCSAR image S, and the calculation expression is $S = \sum_{j=1}^{M-1} S_{j\_new}$.

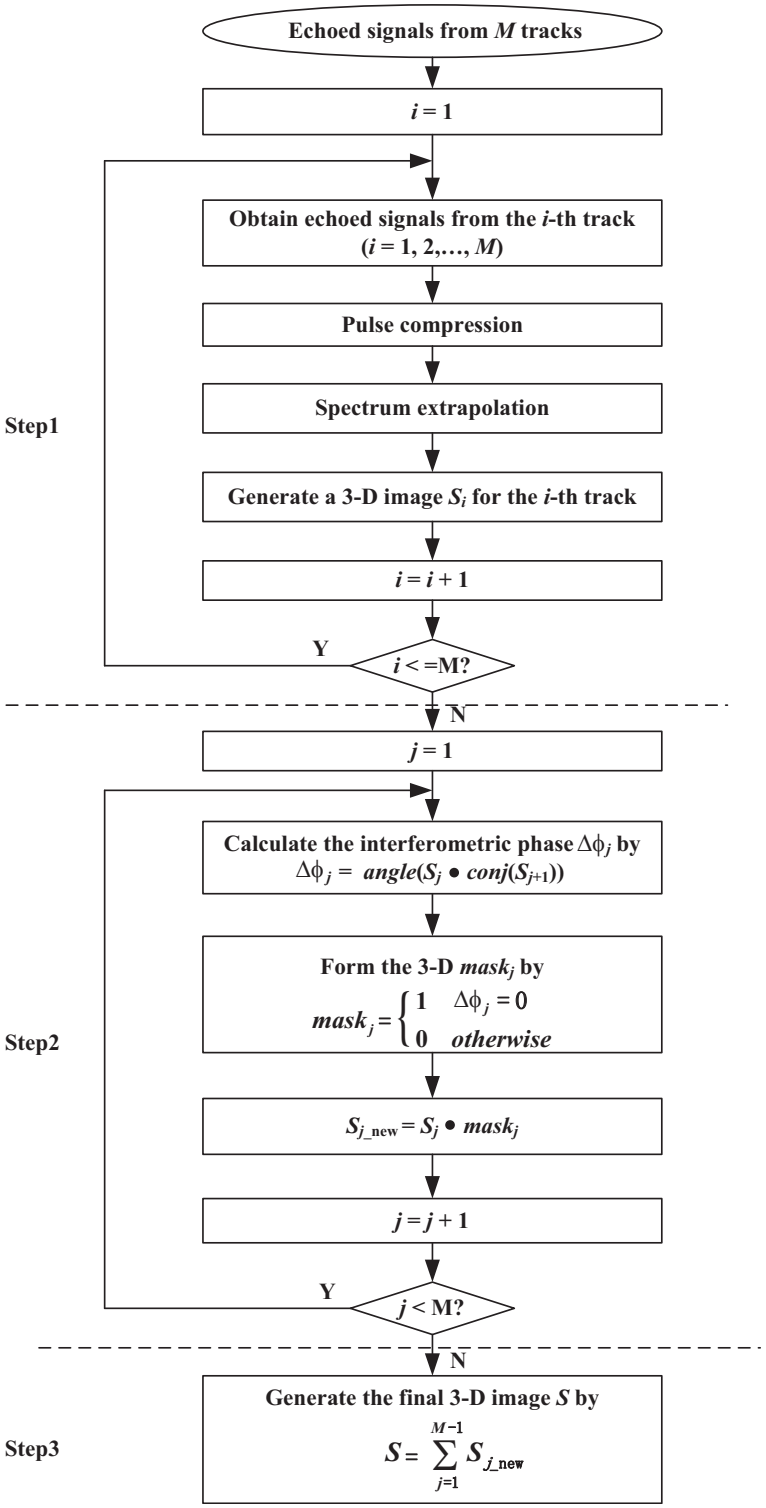

Figure 7. The flow chart of the enhanced 3-D imaging method.

The flow chart of the enhanced 3-D imaging method is shown in Fig. 7. It is obvious that steps (1) and (2) can be processed in parallel for any two-circular tracks data, which is helpful to save computing time.

4. EXPERIMENT RESULTS

Experiments in MCSAR imaging model were performed in an anechoic chamber for a metal tank model, which is shown in Fig. 8. The geometry of data acquisition is shown in Fig. 1 and the parameters of the radar system are shown in Table 1. There are a total of 20 circular tracks.

Table 1. Parameters of radar system.

Carrier frequency	15 GHz
Bandwidth	6 GHz
Radius of radar	8.722 m
Depression angles interval	[8, 11.8] degree
Depression angle sample spacing	0.2 degree

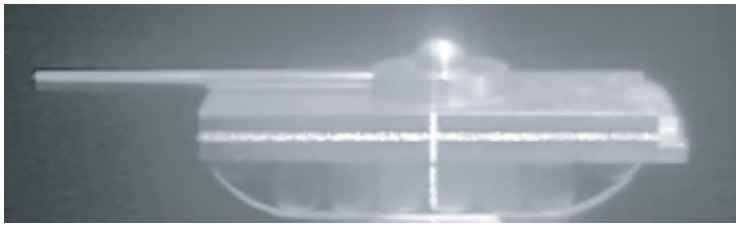

Figure 8. Tank model in an anechoic chamber.

The phase history data of the tank model are shown in Fig. 9(a). When the bandwidth of the observed data is extrapolated from 6 GHz to 10 GHz, the result is shown in Fig. 9(b). Obviously, the spectrum extrapolation is smooth.

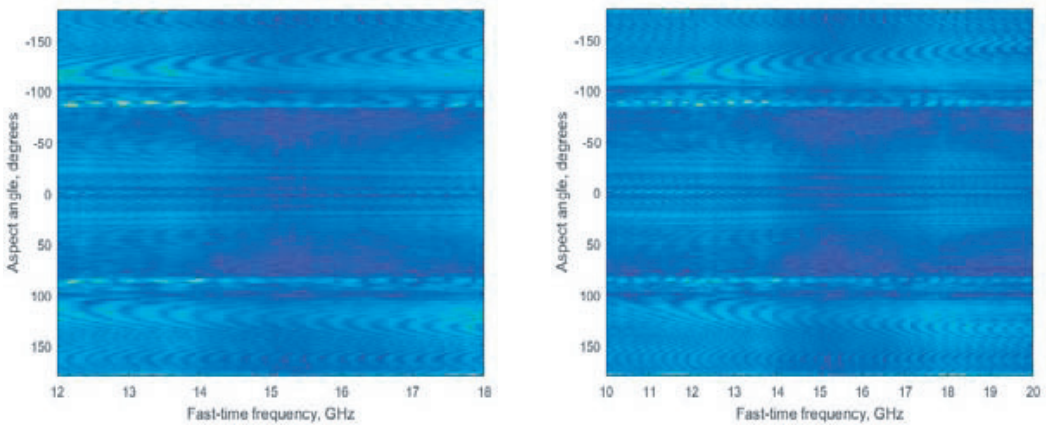

(a) (b)

Figure 9. Phase history data (a) without spectrum extrapolation; (b) with spectrum extrapolation.

The BP algorithm is used in 3-D imaging, and four different imaging cases are considered. (1) 3-D imaging without spectrum extrapolation and without interferometric phase masking, for the echoed signals received from the former 10 tracks; (2) 3-D imaging without spectrum extrapolation and without

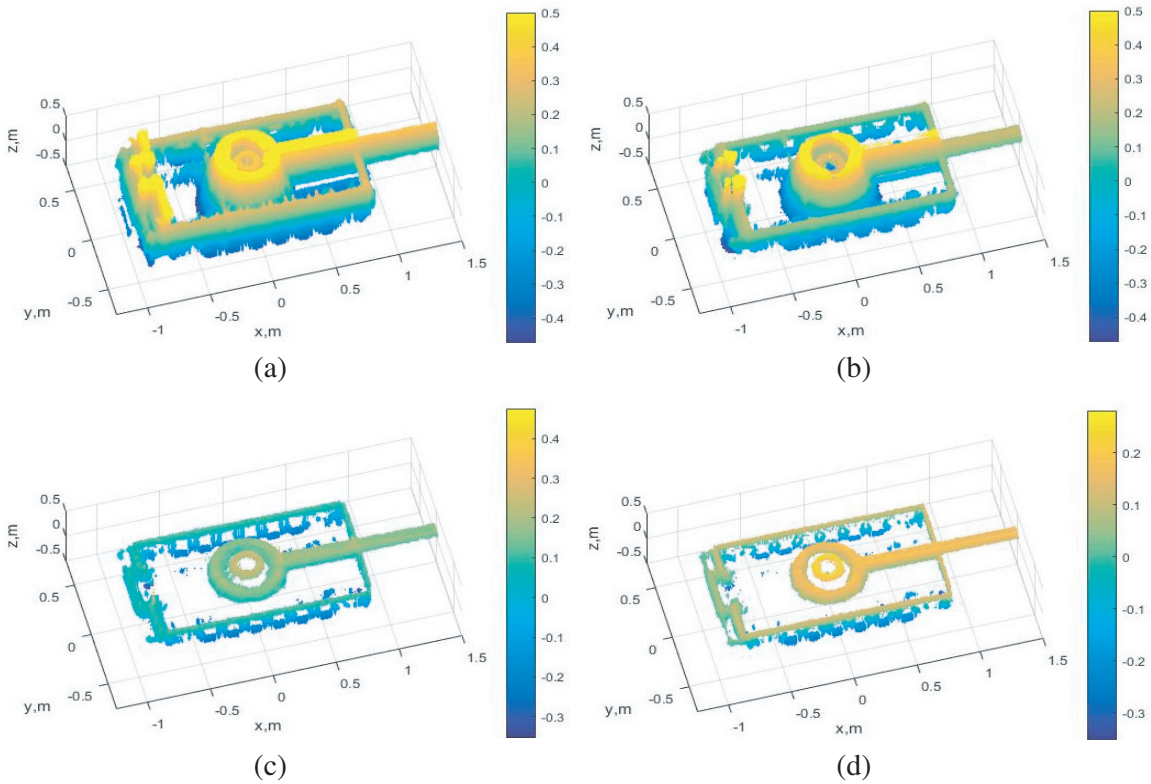

Figure 10. 3-D imaging (a) without spectrum extrapolation and without interferometric phase masking (the number of tracks $M = 10$); (b) without spectrum extrapolation and without interferometric phase masking ($M = 20$); (c) without spectrum extrapolation but with interferometric phase masking ($M = 20$); (d) with spectrum extrapolation and with interferometric phase masking ($M = 20$).

interferometric phase masking, for the echoed signals received from all 20 tracks; (3) 3-D imaging without spectrum extrapolation but with interferometric phase masking, for the echoed signals received from all 20 tracks; (4) 3-D imaging with spectrum extrapolation and with interferometric phase masking, for the echoed signals received from all 20 tracks. These four imaging results are shown in Figs. 10(a)–(d), respectively.

Comparing Fig. 10(a) with (b), the cone-shaped sidelobes and other sidelobes in the x, y, z directions are suppressed because the number of circular tracks is increased from 10 to 20. In Fig. 10(b), the cannon, the body and the wheels of the tank model are clearer than in Fig. 10(a), but they are not well resolved. The cone-shaped sidelobes and other sidelobes still exist.

Comparing Fig. 10(b) with (c), the cone-shaped sidelobes are suppressed very well due to the interferometric phase masking. In Fig. 10(c), the cannon, the body, the wheels and the upper part, including the hemisphere and the cylinder of the tank model, coincide with the theoretical imaging results. Even the gaps between the wheels are clearly visible.

Comparing Fig. 10(c) with (d), the resolution in z direction is improved due to the spectrum extrapolation based on the AR model. In Fig. 10(d), the cannon, the body and the wheels of the tank model are well resolved. The sidelobes between the hemisphere and the cylinder are reduced because the increased spectrum can also suppress PSLR in the x, y directions. The weak edges of the tank back appear as a result of the reduced energy of sidelobes. To be brief, 3-D imaging with spectrum extrapolation and interferometric phase masking can improve the quality of MCSAR imaging effectively.

5. CONCLUSIONS

In this paper, 3-D resolution and cone-shaped sidelobes are analyzed from the spectrum. The results of the analysis show that the imaging quality can be improved by increasing the system bandwidth

and the length of synthetic aperture in the elevation direction. However, it will make the system of acquiring data more difficult. Therefore, an enhanced imaging method based on spectrum extrapolation and interferometric phase masking is presented, which can mainly improve the height resolution and suppress cone-shaped sidelobes. Experimental results focused on the tank model show that this method is effective.

ACKNOWLEDGMENT

This paper was supported by NSFC (61431018, 61501210, and 61571421), Natural Science Foundation of Jiangxi Province (20161BAB202054), Jiangxi University of Science and Technology Research Foundation (NSFJ2014-G22).

REFERENCES

1. Ponce, O., P. Prats, M. Pinheiro, M. Rodriguez-Cassola, R. Scheiber, A. Reigber, and A. Moreira, "Fully polarimetric high-Resolution 3-D imaging with circular SAR at L-band," *IEEE Trans. Geosci. Remote Sens.*, Vol. 52, No. 6, 3074–3090, Mar. 2014.
2. Soumekh, M., *Synthetic Aperture Radar Signal Processing with Matlab Algorithms*, 486–545, Wiley, New York, 1999.
3. Ishimaru, A., T. Chan, and Y. Kuga, "An imaging technique using confocal circular synthetic aperture radar," *IEEE Trans. Geosci. Remote Sens.*, Vol. 36, No. 5, 1524–1530, Sep. 1998.
4. Ponce, O., P. Prats, R. Scheiber, A. Reigber, and A. Moreira, "Analysis and optimization of multi-circular SAR for fully polarimetric holographic tomography over forested areas," *Proc. IEEE Geosci. Remote Sens. Symp.*, 2365–2368, 2013.
5. Austin, C. D., E. Ertin, and R. L. Moses, "Sparse multipass 3D SAR imaging: Applications to the GOTCHA data set," *Proc. SPIE Algorithms for Synthetic Aperture Rdar Imagery XVI*, Vol. 7337, 1–12, 2009.
6. Bryant, M. L., L. L. Gostin, and M. Soumekh, "3-D E-CSAR imaging of a T-72 tank and synthesis of its SAR reconstructions," *IEEE Trans. Aerospace and Electronic Systems*, Vol. 39, No. 1, 211–227, 2003.
7. Ponce, O., P. Prats, R. Scheiber, A. Reigber, and A. Moreira, "First airborne demonstration of holographic SAR tomography with fully polarimetric multicircular acquisitions at L-band," *IEEE Trans. Geosci. Remote Sens.*, Vol. 54, No. 10, 6170–6196, 2016.
8. Ertin, E., R. L. Moses, and L. C. Potter, "Interferometric methods for three-dimensional target reconstruction with multipass circular SAR," *IET Radar, Sonar & Navigation*, Vol. 4, No. 3, 464–473, Jul. 2010.
9. Austin, C. D., E. Ertin, and R. L. Moses, "Sparse signal methods for 3-D radar imaging," *IEEE Journal of Selected Topics in Signal Processing*, Vol. 5, No. 3, 408–423, 2011.
10. Ferrara, M., J. A. Jackson, and C. D. Austin, "Enhancement of multi-pass 3D circular SAR images using sparse reconstruction techniques," *Proc. SPIE. Algorithms for Synthetic Aperture Rdar Imagery XVI*, Vol. 7337, 2009.
11. Yu, L. and Y. Zhang, "CSAR imaging with data extrapolation and approximate GLRT techniques," *Progress In Electromagnetics Research M*, Vol. 19, 209–220, 2011.
12. Lin, Y., W. Hong, W. X. Tan, and Y. R. Wu, "Interferometric circular SAR method for three-dimensional imaging," *IEEE Geosci. Remote Sens. Lett.*, Vol. 8, No. 6, 1026–1030, 2011.
13. Gupta, I. J., M. J. Beals, and A. Moghaddar, "Data extrapolation for high resolution radar imaging," *IEEE Trans. Antennas and Propagation*, Vol. 42, No. 11, 1540–1545, 1994.
14. Kayran, A. H. and I. Erer, "Optimum asymmetric half-plane autoregressive lattice parameter modeling of 2-D fields," *IEEE Trans. Signal Processing*, Vol. 52, No. 3, 807–819, 2004.